

SPADE: Spatial Transcriptomics and Pathology Alignment Using a Mixture of Data Experts for an Expressive Latent Space

Ekaterina Redekop*

University of California, Los Angeles
eredekop@ucla.edu

Zichen Wang

University of California, Los Angeles
zawang0702@ucla.edu

Anthony Sisk

University of California, Los Angeles
asisk@mednet.ucla.edu

Mara Pleasure*

University of California, Los Angeles
mpleasure@ucla.edu

Kimberly Flores

University of California, Los Angeles
kimberlyflores@mednet.ucla.edu

William Speier

University of California, Los Angeles
speier@ucla.edu

Corey W. Arnold

University of California, Los Angeles
cwarnold@ucla.edu

Abstract

The rapid growth of digital pathology and advances in self-supervised deep learning have enabled the development of foundational models for various pathology tasks across diverse diseases. While multimodal approaches integrating diverse data sources have emerged, a critical gap remains in the comprehensive integration of whole-slide images (WSIs) with spatial transcriptomics (ST), which is crucial for capturing critical molecular heterogeneity beyond standard hematoxylin & eosin (H&E) staining. We introduce SPADE, a foundation model that integrates histopathology with ST data to guide image representation learning within a unified framework, in effect creating an ST-informed latent space. SPADE leverages a mixture-of-data experts technique, where experts, created via two-stage feature-space clustering, use contrastive learning to learn representations of co-registered WSI patches and gene expression profiles. Pre-trained on the comprehensive HEST-1k dataset, SPADE is evaluated on 14 downstream tasks, demonstrating significantly superior few-shot performance compared to baseline models, highlighting the benefits of integrating morphological and molecular information into one latent space.

1. Introduction

High-resolution whole slide images (WSIs) have propelled the development of powerful deep learning foundation models in computational pathology, demonstrating robust performance across diverse tissue types and tasks [10, 15, 25, 29]. These models excel in various applications, from cancer subtype classification to patient outcome prediction.

Due to their gigapixel resolution and limited pixel-level annotations, WSIs are typically processed as patches. Standard practice is to use multiple instance learning (MIL), which utilizes weak slide-level labels [4] and involves embedding individual patches with a pre-trained model and then aggregating these embeddings for downstream tasks. This approach relies on high-quality patch embeddings, driving the development of self-supervised foundation models in digital pathology [5, 6, 28, 32]. When applied to images or paired data from multiple modalities, self-supervised learning produces diverse, expressive feature encoders and enables training on large unlabeled datasets spanning multiple organs. These task-agnostic self-supervised encoders are robust to institutional variations, including differences in staining procedures and other image-quality factors. [5, 6, 28, 32].

By visually capturing cellular arrangement, WSIs enable the study of spatial organization and disorganization of cells in tissues, characterizations that are especially relevant in cancer research [20, 21]. In clinical settings, WSIs are com-

* Indicates shared first authorship

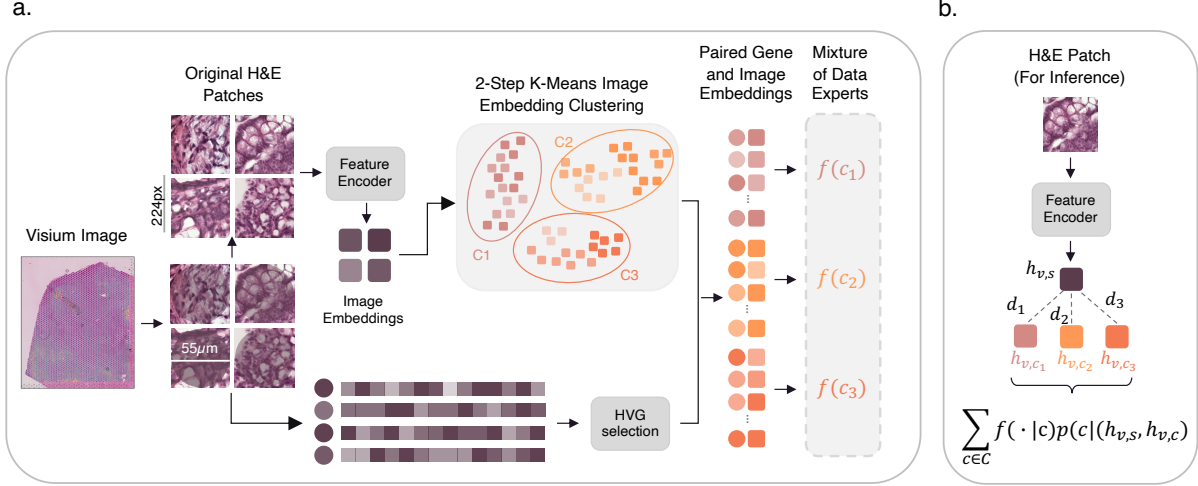


Figure 1. **Overview of SPADE workflow.** **a.** A WSI is segmented and patched into a set of non-overlapping patches. A compressed feature for each patch is obtained through a pre-trained feature encoder. A corresponding gene expression vector is obtained after preprocessing. 2-step K-Means clustering is performed to create data experts across all WSIs in the dataset. **b.** For inference, three data experts’ routing techniques are evaluated (Section.3.4).

monly stained with hematoxylin & eosin (H&E), a two-color stain that highlights nuclei and cytoplasm but offers a limited view of molecular-level heterogeneity [14]. As tumor tissues are known to exhibit high variability within and across patients, deciphering the heterogeneity at the molecular level is critical for improving deep learning applications that can more precisely inform diagnosis, treatment, and prognosis [24, 33]. While H&E provides crucial morphological insights, its inability to capture molecular heterogeneity limits its utility in fully characterizing tissue complexity.

Spatial transcriptomics addresses this gap by providing spatially resolved gene expression data, allowing for additional molecular context for a given tissue specimen. Although both ST and H&E data have independently proven useful in various applications, their combined potential for creating a more comprehensive representation learning framework remains unexplored. To this end, we introduce SPADE, a vision-ST foundation model that uses a mixture of experts, each trained via contrastive learning, to unify ST data and H&E images to produce slide representations that encompass both modalities. SPADE is trained using a large collection of Visium data from the HEST-1K dataset to generate a rich, expressive latent representation space that spans multiple tissue types [12]. We hypothesize that training a contrastive learning model on paired ST and WSI data will create a shared latent space that captures molecularly informed features of tissue organization. This enriched representation is expected to improve performance across various downstream tasks compared to conventional WSI self-supervised

learning.

SPADE’s novel architecture based on a mixture-of-experts is specifically designed to handle the complexities of spatially resolved paired ST and H&E data. Each expert is trained on a distinct subset of ST-WSI pairs, identified through a two-step K-means clustering process. First, patches are grouped into K subclusters within each organ, yielding per-organ centroids. Then, these centroids are clustered again across all organs to arrive at a final set of K representative clusters spanning the 515 Visium WSIs. This process generates hard negatives, enhancing training for individual experts and ensuring robust representation learning across multiple tissue types. Our contributions are summarized as follows:

1. **Multimodal Representation Learning:** We propose the first histology foundation model that pretrains on paired H&E and ST data, producing an enriched latent space for pathology tasks.
2. **Mixture-of-Experts with Hard Negative Mining:** By clustering WSIs in a two-step K-means process, SPADE identifies challenging examples that enhance discrimination and prevent trivial solutions, especially across diverse organ types.
3. **Comprehensive Evaluation across 14 Tasks:** We demonstrate SPADE’s effectiveness on eight cancer classification tasks and six survival prediction tasks, showcasing its robust performance in modeling the complexity of tumor samples.

2. Related work

2.1. Contrastive learning pretraining for multimodal datasets

Contrastive learning is a core self-supervised approach for large imaging datasets, which uses the InfoNCE loss, introduced by van den Oord et al. [22], to pull positive pairs of data points closer together while pushing negative pairs apart. Contrastive language-image pretraining (CLIP) extends this technique to multimodal data by using paired images and captions [23]. Rather than focusing solely on images, CLIP creates a multimodal embedding space using a symmetric InfoNCE loss that matches paired images and captions as positives and mixes random images and captions as negatives. This symmetric process (image-to-caption and caption-to-image) allows CLIP to develop a latent space where images and their corresponding captions cluster together. BLEEP applies the CLIP framework to spatial transcriptomics for gene expression prediction, creating a multimodal model specifically for Visium data but trained on a single tissue type, limiting its generalizability. Another model, TANGLE, recently developed by Jaume et al. [13] applies the CLIP framework to paired H&E WSIs and bulk RNA-seq data from the Cancer Genome Atlas (TCGA); however, bulk RNA sequencing requires tissue dissociation and lacks the spatial resolution present in each WSI. SPADE addresses these limitations by training on multiple tissue types using a Mixture-Of-Experts approach, utilizing paired H&E and ST data at the patch level to learn rich spatially-informed patch-level embeddings for multiple tissue types.

2.2. Clustering for non-trivial contrastive learning

SPADE is trained on a dataset that spans multiple organs leading to a risk of the original CLIP framework finding trivial solutions by contrasting different tissue types with each other instead of learning a meaningful latent space. Because CLIP samples negative pairings from within each batch, highly varied images in a batch can make these pairings easier for the model to learn. Ma et al. proposed a Mixture of Data Experts (MoDE) approach to address the limitations of CLIP using non-trivial negative pairings to train by incorporating a two-step K-means clustering process into training [19]. MoDE first clusters semantically similar text captions, then trains a distinct CLIP model within each cluster. By sampling hard negatives from within these similar groups, the model is forced to focus on distinguishing features that differentiate similar captions and their paired images [19].

Using a two-step K-means procedure, we adapt this hard-negative sampling procedure to Visium data and cluster in the image feature space. In [27] the authors demonstrate how hierarchical clustering can be leveraged to create high-quality representations by progressively refining clusters at

different levels of abstraction. Inspired by this, our two-step K-means procedure first clusters data within each organ type, and then clusters the resulting organ-specific centroids. This allows our model to learn a more detailed and expressive latent space for each expert while also allowing flexibility to work across cancer types and vastly different tissue makeups.

3. Method

We present our framework: SPADE, Spatial transcriptomics and Pathology Alignment using a mixture of Data Experts. (Figure 1). The proposed framework acts as an image encoder, where the extracted embeddings are subsequently aggregated to generate a comprehensive slide-level representation. The proposed framework comprises a mixture of data experts $\{f(\cdot|c)\}$ (Section 3.3), where each data expert $f(\cdot|c)$ is a CLIP-based model trained on the cluster c (Section 3.2) using a contrastive objective to align an H&E patch embedding with a gene expression embedding (Section 3.1). SPADE is tested on a variety of downstream tasks (Section 4.4). Additional details can be found in **Supplementary Materials**.

3.1. Background: Basic contrastive pretraining

SPADE utilizes a contrastive learning framework inspired by CLIP, designed with a modified loss function to learn a bimodal embedding that aligns image patches with their corresponding gene expression data [31]. In contrast to natural images, it is common to sample multiple spots with similar gene expression profiles or image morphological features within the same batch, which the contrastive objective should not pull apart. To take into account similar pairs, the similarity-adjusted target t is computed as follows:

$$t = \frac{\sigma(\text{sim}(h_x, h_x) + \text{sim}(h_v, h_v))}{2} \cdot \tau \quad (1)$$

where h_v is an m -dimensional image embedding, h_x is an m -dimensional gene expression embedding, and τ - temperature parameter. The contrastive objective \mathcal{L} is then updated to align h_v and h_x in the latent space and is computed with cross-entropy (CE) as follows:

$$\mathcal{L} = \text{mean} \left(\text{CE}(\text{sim}(h_v, h_x), t) + \text{CE}(\text{sim}(h_v, h_x)^\top, t^\top) \right) \quad (2)$$

3.2. Clustering

Each WSI $X_j, j = 1, \dots, J$ from the pretraining cohort \mathcal{D} of size J is divided into a set of non-overlapping patches $X_j = \{x_j^1, \dots, x_j^{N_j}\}$, where each patch $x_j^n \in \mathbb{R}^{W \times H \times 3}$. A feature encoder $f_{\text{enc}}(\cdot)$ pre-trained on a large cohort of histopathology data is then used to extract a compressed embedding from each patch. This results in a set of embed-

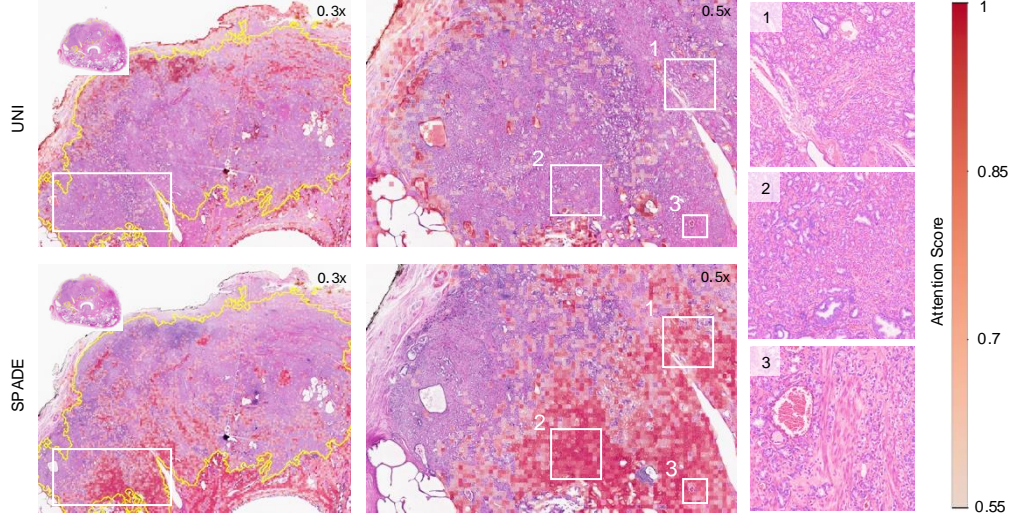


Figure 2. **Interpretability of SPADE.** Attention scores for a prostate WSI positive for biochemical recurrence (BCR) are visualized as a heatmap for the UNI and SPADE models. The deeper the red color the higher attention the model put on that region of the tissue. The yellow outline shows the predicted tumor boundary. SPADE shows higher concentration of attention within the tumor boundary. Sub-crops are selected to show the patterns with high-attention at higher magnifications.

dings $H_{v,j} = \{h_{v,j}^1, \dots, h_{v,j}^{N_j}\}$ where $h_{v,j}^n = f_{\text{enc}}(x_j^n) \in \mathbb{R}^m$.

The goal is to extract a set of image clusters $\{h_{v,1}, \dots, h_{v,C}\}$ with $h_{v,c} \in \mathbb{R}^m$ based on the set of patch-level embeddings to formulate conditions C for data expert training. To train these experts, we utilize a two-step K-means clustering approach. In the first step, we apply fine-grained clustering utilizing patch-based embeddings within each organ type to identify clusters where the samples share similar semantics. In the second step, we aggregate the fine-grained clusters based on each cluster’s centroid to establish coarse-grained clustering, facilitating specialization among data experts across different organs.

Given the large size of the pretraining dataset \mathcal{D} , K-means is performed on a subset of the data, as training K-means on the entire dataset may be computationally inefficient. We draw a uniform sample from each organ-specific subset (32 organs in total): $\mathcal{D}_i \sim \mathcal{D}_i$ and $|\mathcal{D}_i| \ll |\mathcal{D}|$, where $1 \leq i \leq 14$. Then fine-grained K-means is performed over each \mathcal{D}_i :

$$S_i \leftarrow \text{K-means}(\mathcal{D}_i) \quad (3)$$

, where $S = \bigcup S_i$ - set of learned cluster centers.

A second round of clustering is performed on top of previously found cluster centers S :

$$C \leftarrow \text{K-means}(S) \quad (4)$$

, where each $c \in C$ becomes a condition for a data expert $f(\cdot|c)$.

To determine the optimal number of clusters for both steps, we performed a within-cluster sum of squares (WCSS) analysis and used the elbow method to identify the point where adding more clusters provided diminishing returns. This ensured that our clustering approach captured meaningful biological variation while avoiding excessive fragmentation of the data

3.3. Data Experts Training

In this work, we propose to train a set of CLIP models $\{f(\cdot|c)\}$ independently given clusters C , such that $c \in C$. The training data for a data expert $\{f(\cdot|c)\}$ is :

$$\mathcal{D}_c = \bigcup_{s \in S_c} \mathcal{D}_s \quad (5)$$

, where $\mathcal{D}_s = \{d | s = \text{argmin}_{s \in S} (\|h_{v,s} - h_{v,c}\|_2^2, d \in \mathcal{D})\}$ is the data assigned for each fine-grained cluster with $h_{v,s}$ and $h_{v,c}$ being the image embeddings for training example s and fine-grained cluster center c respectively. S_c is a set of fine-grained clusters assigned to each data expert $f(\cdot|c)$, further trained only on \mathcal{D}_c .

3.4. Slide-level Representation

The proposed experts-based approach provides multiple patch-based models to select from during inference rather than relying solely on a single CLIP model. We evaluate three distinct weighting techniques for routing data experts

	Lung				Prostate				Lymph Nodes		Ovarian		Breast			
	PLCO		CPTAC		PANDA		TCGA-PRAD		CAM16		UBC-OCEAN		PLCO		TCGA-BRCA	
	AUC	F1	AUC	F1	AUC	F1	AUC	F1	AUC	F1	AUC	F1	AUC	F1	AUC	F1
TANGLE	95.9	91.1	96.7	96.6	88.1	57.4	-	-	74.2	57.9	96.4	81.5	76.4	55.3	-	-
GigaPath	97.0	<u>90.1</u>	97.1	89.9	72.5	33.9	75.3	38.7	93.0	<u>88.3</u>	94.2	77.9	69.6	50.4	69.4	63.9
UNI+ABMIL	97.1	89.3	96.9	88.8	<u>93.2</u>	<u>66.8</u>	<u>81.0</u>	<u>52.7</u>	96.0	81.7	97.8	89.1	<u>79.7</u>	<u>55.0</u>	97.5	97.1
CONCH+ABMIL	97.0	91.3	96.7	88.8	90.9	62.3	78.9	47.9	81.8	74.4	96.5	82.9	76.7	51.6	98.3	96.7
SPADE+ABMIL	98.5	87.1	<u>97.9</u>	92.5	94.9	74.7	82.1	56.9	98.6	89.1	97.8	<u>87.1</u>	82.1	57.3	97.7	98.9
UNI+TransMIL	97.0	77.8	93.1	82.1	92.1	64.8	76.2	47.5	<u>96.9</u>	85.7	97.1	82.0	70.4	47.3	<u>97.8</u>	97.3
CONCH+TransMIL	<u>98.3</u>	89.3	98.1	<u>91.3</u>	92.1	63.8	80.9	46.8	96.3	<u>88.3</u>	95.7	83.6	76.9	53.8	97.2	95.9
SPADE+TransMIL	96.6	82.0	94.6	89.7	91.7	62.5	72.0	43.9	93.4	82.9	<u>97.3</u>	83.1	72.5	47.9	97.3	<u>97.5</u>

Table 1. **Subtyping prediction** results of SPADE and baselines for eight different subtyping tasks. Metrics AUC and F1 are shown as percentages. The best performance is in bold, and the second best is underlined. TANGLE could not be applied to TCGA datasets since they were used to train the model.

by formulating their outputs as a weighted sum for simplicity:

$$\sum_{c \in C} f(\cdot|c) \cdot p_i(c|(h_{v,s}, h_{v,c})) \quad (6)$$

, where $p_i(c|(h_{v,s}, h_{v,c}))$ represents the normalized weight assigned to each expert, satisfying $\sum_{c \in C} p_i(c|(h_{v,s}, h_{v,c})) = 1$. Here, $i \in 1, 2, 3$ denotes three weighting techniques being compared, $h_{v,s}$ is the sample’s image embedding, and $h_{v,c}$ is the expert’s centroid. In the first approach, each data sample is routed to a single expert based on the proximity of its embedding to the expert centroids. Specifically:

$$p_1(c|(h_{v,s}, h_{v,c})) = \begin{cases} 1 & \text{if } c = \arg \min_{c' \in C} d_{c'} \\ 0 & \text{otherwise} \end{cases} \quad (7)$$

, where $d_{c'} = (\|h_{v,s} - h_{v,c'}\|_2^2)$. In the second approach, the outputs from all experts are averaged for each data sample:

$$p_2(c|(h_{v,s}, h_{v,c})) = \frac{1}{C} \quad (8)$$

In the third approach, the outputs of all experts are combined using a normalized weighted sum, with the weights being inversely proportional to the distance from the data sample to each expert’s centroids:

$$p_3(c|(h_{v,s}, h_{v,c})) = \frac{\bar{d}_c}{\sum_C \bar{d}_i}, \bar{d}_c = \frac{1}{d_c} \quad (9)$$

After features are obtained for each patch, a slide-level feature vector can be derived through a learnable aggregation method. Specifically, we employed Attention-Based Multiple Instance Learning (ABMIL) [11] and Transformer-based Multiple Instance Learning (TransMIL) [26], which

allow for aggregating patch-level embeddings into a slide-level representation. In this setup, each patch embedding is treated as an instance, and the model learns to assign attention weights to each instance based on its relevance to the slide-level prediction task. ABMIL leverages an attention mechanism to weight each patch’s contribution, capturing spatial heterogeneity across the slide. In contrast, TransMIL uses transformer-based self-attention layers to capture dependencies between patches, allowing for more complex interactions and relationships to be modeled. The resulting slide-level feature vector can then be utilized for various downstream tasks, as described in Section 4.1.

4. Experiments and Results

4.1. Datasets

Each dataset was processed in a similar manner with a fixed stain normalization and 224×224 patching at magnification 20x. The Visium gene expression data was processed by normalizing each spot to its total count, followed by log normalization. Subsequently, highly variable genes were identified using the Scanpy package [30]. The union of the top 50 most highly variable genes from each sample was used for training and prediction, resulting in 7,986 genes following the method outlined in [31]. Additional details can be found in **Supplementary Materials**.

Pretraining For pretraining, we utilized the HEST-1k dataset, a diverse collection of 1,229 spatial transcriptomic profiles, each paired with a WSI. HEST-1k spans 153 cohorts, covering 26 organs, and includes 367 cancer samples across 25 types. For this work, we utilized only the Homo sapiens samples obtained using Visium technology, leading to a total of 515 profiles.

Subtyping We evaluated the proposed approach on six dif-

	Prostate BCR		Lung	Uterine	Breast	
	Private	TCGA-PRAD	PLCO	TCGA-UCEC	TCGA-BRCA	PLCO
	c-index	c-index	c-index	c-index	c-index	c-index
TANGLE	60.3	-	48.6	-	-	57.0
GigaPath	66.4	53.0	59.5	69.1	65.5	56.0
UNI+ABMIL	58.8	56.5	57.8	64.6	74.1	56.0
CONCH+ABMIL	60.3	55.9	35.8	64.5	64.5	55.5
SPADE+ABMIL	<u>67.0</u>	59.4	<u>64.7</u>	72.4	71.8	59.5
UNI+TransMIL	56.5	57.7	58.4	<u>72.2</u>	70.3	54.2
CONCH+TransMIL	52.5	53.0	46.8	65.9	65.9	54.7
SPADE+TransMIL	71.4	<u>58.8</u>	72.3	71.0	<u>73.0</u>	<u>57.4</u>

Table 2. **Survival and BCR prediction** results of SPADE and baselines for six different subtyping tasks. c-index values are shown as percentages. The best performance is in bold, and the second best is underlined. TANGLE could not be applied to TCGA datasets since they were used to train the model.

	Lung				Prostate		Lymph Nodes		Ovarian		Breast	
	PLCO		CPTAC		PANDA		CAM16		UBC-OCEAN		PLCO	
	AUC	F1	AUC	F1	AUC	F1	AUC	F1	AUC	F1	AUC	F1
p_1 +ABMIL	97.9	85.0	97.1	91.1	94.4	71.6	97.1	87.5	96.8	76.9	79.3	51.4
p_2 +ABMIL	97.6	95.2	<u>97.7</u>	90.4	94.0	71.1	93.6	77.6	97.2	80.0	76.6	<u>55.6</u>
p_3 +ABMIL	98.5	<u>87.1</u>	97.9	92.5	94.9	74.7	98.6	89.1	97.8	87.1	82.1	57.3
p_1 +TransMIL	<u>96.5</u>	<u>82.0</u>	<u>95.4</u>	<u>86.0</u>	88.9	55.7	77.7	67.5	95.0	75.9	70.7	47.6
p_2 +TransMIL	91.4	70.0	94.9	85.7	<u>90.2</u>	<u>59.9</u>	<u>92.9</u>	83.0	<u>96.4</u>	<u>82.9</u>	77.8	54.0
p_3 +TransMIL	97.4	93.0	96.3	89.7	91.7	62.5	93.4	<u>82.9</u>	97.3	83.1	<u>72.5</u>	<u>47.9</u>

Table 3. **Ablation study of the data experts’ routing method for subtyping.** p_1 corresponds to the case where the expert associated with the closest centroid is selected for each data point. p_2 corresponds to the case where the outputs of all experts are averaged to produce a final prediction. p_3 corresponds to the case where the expert selection is inversely proportional to the distance (Section 3.4). Metrics AUC and F1 are shown as percentages. The best performance is in bold, and the second best is underlined.

ferent subtyping tasks: Non-Small Cell Lung Carcinoma (NSCLC) subtyping on PLCO [34] and CPTAC [9] (two classes), ISUP grading based on Prostate cancer grade assessment (PANDA) challenge [3] (six classes), classification of breast cancer metastases in lymph nodes (Cameleon16) [2, 16] (three classes), ovarian cancer subtypes classification (UBC-OCEAN) challenge [1, 8] (five classes), and PLCO Breast cancer subtyping classification (three classes) [34]. For each dataset where patient identifiers were provided, all patient WSIs were aggregated into one set of vectors for input to ABMIL and TransMIL.

Survival We evaluated the proposed method on four different survival tasks: Breast Invasive Carcinoma (BRCA) from TCGA and PLCO, Non-Small Cell Lung Carcinoma (NSCLC) from PLCO, and Uterine Corpus Endometrial Carcinoma (UCEC) from TCGA.

Prostate Cancer Biochemical Recurrence We evaluated the proposed solution on two different prostate cancer datasets, one public coming from TCGA (TCGA-PRAD) and one private dataset coming from our institution.

4.2. Baselines and Ablations

We compared our approach against three baseline encoders: UNI, TANGLE (pancancer-trained) (Section 2), CONCH [18] and Prov-GigaPath [32]. We assessed two distinct aggregation mechanisms for slide-level features: ABMIL and TransMIL.

Unlike the other methods, TANGLE provides a direct slide-level vector representation, eliminating the need for patch-level aggregation. For TANGLE, we evaluated the model with linear probing on the slide-level features to assess its performance on downstream tasks.

Alongside the baseline comparisons, we conducted an ablation study to compare methods for routing data experts (Section 3.4). Additionally, we conducted an ablation study to experiment with different numbers of clusters in both the initial and second steps of clustering. Lastly, we implemented a version of SPADE with one-step K-means clustering to evaluate the effect of the additional clustering step on downstream performance (see **Supplementary Materials**).

To thoroughly evaluate SPADE, we conducted a comparison with a single-expert model (SPADE-0) across subtyping, survival, and BCR prediction tasks (see **Supplementary Materials**).

4.3. Implementation Details

We used publicly available implementations and pre-trained weights for all baseline foundational models in our study. The preprocessing pipelines were adopted from the official repositories of each model, ensuring consistency with their original training procedures. No additional fine-tuning or retraining was performed on these models beyond their publicly released checkpoints.

For the classification ABMIL and TransMIL models, we trained them from scratch using the same set of hyperparameters across all downstream experiments (see **Supplementary Materials**)

4.4. Results

4.4.1. Cancer Subtyping

The SPADE framework consistently outperforms baseline models across a range of cancer subtyping tasks, showing clear advantages in both AUROC and F1-score metrics. Notably, SPADE achieves the highest AUC across six out of eight tasks and secures the highest F1 score for six of the tasks (Table 1). CONCH features led to higher AUC for lung (CPTAC) and breast (TCGA-BRCA) subtyping tasks, as well as higher F1 score for lung subtyping (PLCO). UNI features resulted in a higher F1 score for the ovarian cancer subtyping task (UBC-OCEAN). The comparison with TANGLE’s performance highlights the distinct advantage of spatial transcriptomics over Bulk RNA-seq. Using Bulk RNA-seq may limit model expressibility, likely due to the loss of heterogeneity and the lack of one-to-one alignment between expression and imaging data.

4.4.2. Survival Prediction and Prostate BCR Analysis

We used the concordance index (c-index) for survival and prostate cancer biochemical recurrence (BCR) evaluation (Table 2). To overcome the limitations of overall survival, which includes deaths unrelated to cancer, we utilize disease-specific survival (DSS) for the four survival tasks [17].

SPADE outperforms all baseline models, achieving the highest c-index for three out of the four survival tasks and all BCR prediction tasks. In the TCGA-BRCA survival task, UNI surpasses SPADE, but SPADE still achieves the second-highest performance. SPADE outperforms TANGLE on all datasets, demonstrating the critical importance of spatial context in modeling disease progression, which is achieved by incorporating ST data.

4.4.3. Ablation Studies

For the data experts’ routing ablation studies, there is varying performance between different routing techniques (Table 3, 4). For most subtyping datasets, p_2 (averaging) and p_3 (distance weighting) routing methods perform better than p_1 , which simply uses the expert of the closest centroid. This indicates the additional model input from other experts provides a performance advantage, perhaps allowing for more complex representations of the WSI.

Our ablation study on the two-step clustering procedure revealed that varying the number of clusters at each stage (k_1 and k_2) can influence the model performance, but the improvement varies across different datasets and cancer types (see Table 5, 6). For the subtyping task, the configuration with $k_1 = 16, k_2 = 16$ using ABMIL achieved the highest AUC in five datasets, demonstrating the effectiveness of balanced hierarchical clustering. Increasing the second-stage clustering granularity ($k_2 = 32$) improved F1 scores in several cases, such as lung PLCO, ovarian, and breast TCGA-BRCA, suggesting that a finer-grained latent space can enhance classification precision, but it also requires double the computation resources or double the runtime. Reducing the second-stage clustering granularity ($k_2 = 8$) led to mixed results: while it improved F1 in some datasets, it generally resulted in lower AUC scores.

For the survival and BCR, $k_1 = 16, k_2 = 16$ achieved the highest c-index with ABMIL and TransMIL, demonstrating the effectiveness of balanced clustering. Increasing k_1 and k_2 to 32 improved the c-index for TCGA-BRCA while reducing k_2 to 8 led to performance drops across all survival tasks.

Further comparisons between SPADE and its single-expert version highlight the significant impact of the mixture of data experts module on the performance, as evidenced by SPADE’s consistently higher AUC and F1 score (see **Supplementary Materials**). This trend may be attributed to the diverse tissue types represented in the HEST-1k dataset (e.g. brain, heart, lung). A model trained on all organ types might lack the specificity needed to improve performance for each task. Given the high variability of genes present between tissue types, training on data from all organs within a single model may limit its ability to capture the heterogeneity essential for effective subtyping and survival prediction. Additionally, as discussed in Section 2.2, with such diverse tissue types, contrastive learning could rely on easy negative pairings to drive down the loss, resulting in a less expressive latent space.

4.4.4. Interpretability Analysis

We conducted interpretability analyses by plotting the attention weights from the ABMIL variants on our in-house Prostate BCR dataset to better understand the differences

	Prostate BCR		Lung	Uterine	Breast	
	Private	TCGA-PRAD	PLCO	TCGA-UCEC	TCGA-BRCA	PLCO
	c-index	c-index	c-index	c-index	c-index	c-index
p_1 +ABMIL	63.7	57.6	56.6	70.7	68.3	56.6
p_2 +ABMIL	<u>66.8</u>	<u>59.0</u>	<u>57.8</u>	<u>71.5</u>	<u>69.5</u>	<u>57.0</u>
p_3 +ABMIL	67.0	59.4	64.7	72.4	71.8	59.5
p_1 +TransMIL	66.2	57.9	67.7	70.2	69.4	517
p_2 +TransMIL	<u>69.7</u>	<u>58.1</u>	<u>71.7</u>	<u>70.4</u>	<u>71.6</u>	<u>52.9</u>
p_3 +TransMIL	71.4	58.8	72.3	71.0	71.8	56.9

Table 4. **The ablation study of the data experts’ routing method for survival and BCR.** p_1 corresponds to the case where the expert associated with the closest centroid is selected for each data point. p_2 corresponds to the case where the outputs of all experts are averaged to produce a final prediction. p_3 corresponds to the case where the expert selection is inversely proportional to the distance (Section 3.4). The best performance is in bold, and the second best is underlined. c-index values are shown as percentages.

	Lung				Prostate				Lymph Nodes		Ovarian		Breast			
	PLCO		CPTAC		PANDA		TCGA-PRAD		CAM16		UBC-OCEAN		PLCO		TCGA-BRCA	
	AUC	F1	AUC	F1	AUC	F1	AUC	F1	AUC	F1	AUC	F1	AUC	F1	AUC	F1
$16(k_1), 16(k_2), \text{ABMIL}$	98.5	87.1	97.9	92.5	94.8	74.7	82.1	56.9	98.7	89.1	97.8	87.1	82.1	57.3	97.7	99.0
$16(k_1), 8(k_2), \text{ABMIL}$	96.8	91.3	97.3	89.6	94.4	76.0	81.4	49.3	93.6	87.3	<u>97.7</u>	85.3	80.3	58.6	97.4	98.0
$16(k_1), 32(k_2), \text{ABMIL}$	<u>97.8</u>	95.45	98.1	90.2	94.6	71.2	81.4	51.1	98.7	90.5	<u>97.4</u>	88.0	78.6	57.6	97.5	99.1
$32(k_1), 32(k_2), \text{ABMIL}$	97.2	87.8	96.9	84.6	94.1	69.7	83.5	50.8	98.6	91.1	96.9	78.3	<u>77.5</u>	<u>58.4</u>	97.8	99.3
$16(k_1), 16(k_2), \text{TransMIL}$	96.5	82.0	96.3	89.7	89.5	58.9	72.0	43.9	93.4	82.9	97.3	83.5	72.5	47.9	97.3	98.7
$16(k_1), 8(k_2), \text{TransMIL}$	94.1	83.7	93.5	85.3	89.9	54.6	78.1	30.5	91.3	80.3	97.4	83.1	78.0	55.4	97.0	96.8
$16(k_1), 32(k_2), \text{TransMIL}$	96.3	87.8	94.0	83.5	88.0	54.6	77.2	31.8	94.5	85.4	97.6	82.5	75.1	58.3	<u>97.7</u>	<u>99.2</u>
$32(k_1), 32(k_2), \text{TransMIL}$	95.9	82.0	94.2	85.7	94.1	69.7	78.4	30.7	97.6	<u>91.0</u>	97.9	87.4	77.3	56.2	97.4	98.7

Table 5. **Ablation study of the number of experts for each clustering step for subtyping.** Metrics AUC and F1 are shown as percentages. The best performance is in bold, and the second best is underlined.

between the SPADE and UNI features. In Figure 2, we present attention heatmaps, where deeper red indicates higher attention weights, and the predicted cancer mask is shown in yellow. We validated this cancer prediction mask against pathology reports. In panel (a), UNI attention highlights some small regions within the tumor boundary, but much of the attention is diffuse. In contrast, the SPADE-N framework’s attention weights display higher attention regions within the cancer region and a hot zone along the bottom right border of the tumor mask.

The heatmap 2 depicts what regions of the WSI had the highest attention for a case from the in-house BCR task. The attention heatmap produced by SPADE highlights areas predominantly showing poorly formed and compact $4 + 5$ and $4 + 3$ tumor patterns with tertiary 5 according to the Gleason grading system [7], subtle desmoplastic stromal response with slightly cellular fibroblasts exhibiting pale cytoplasm and nuclear enlargement.

5. Conclusions

Based on the performance across our 14 downstream tasks, the SPADE framework has shown to be an expressive feature encoder using spatial transcriptomics data. Utilization of HEST-1k allowed our model to learn robust, biologically relevant embeddings by aligning histological image features with spatially resolved gene expression patterns, which set a strong foundation for downstream pathology analysis tasks. Our improved performance over the single expert version of our framework highlights the benefit of SPADE’s mixture of experts approach. Additionally, our results show significant improvement over TANGLE, which relies on bulk sequencing data, underscoring the value of spatial gene profiling. SPADE’s ability to utilize spatial context allows our model to capture localized differences in gene expression that are crucial for accurate disease subtyping and survival prediction.

References

- [1] Maryam Asadi-Aghbolaghi, Hossein Farahani, Allen Zhang, Ardalan Akbari, Sirim Kim, Ashley Chow, Sohler Dane,

	Prostate BCR		Lung	Uterine	Breast	
	Private	TCGA-PRAD	PLCO	TCGA-UCEC	TCGA-BRCA	PLCO
	c-index	c-index	c-index	c-index	c-index	c-index
$16(k_1), 16(k_2), \text{ABMIL}$	67.0	59.4	64.7	72.4	71.8	59.5
$16(k_1), 8(k_2), \text{ABMIL}$	66.2	55.7	53.2	70.4	70.8	56.1
$16(k_1), 32(k_2), \text{ABMIL}$	70.2	57.4	60.7	71.7	71.7	57.0
$32(k_1), 32(k_2), \text{ABMIL}$	68.9	56.5	56.5	72.1	72.0	57.2
$16(k_1), 16(k_2), \text{TransMIL}$	71.4	<u>58.8</u>	72.3	71.0	71.8	56.9
$16(k_1), 8(k_2), \text{TransMIL}$	65.3	52.9	61.4	68.9	70.7	52.9
$16(k_1), 32(k_2), \text{TransMIL}$	65.8	52.5	62.4	70.6	71.1	52.5
$32(k_1), 32(k_2), \text{TransMIL}$	<u>70.4</u>	55.9	63.0	70.8	71.2	55.9

Table 6. **Ablation study of the number of experts for each clustering step for survival and BCR.** c-index values are shown as percentages. The best performance is in bold, and the second best is underlined.

- OCEAN Challenge Consortium, OTTA Consortium, David G Huntsman, et al. Machine learning-driven histotype diagnosis of ovarian carcinoma: Insights from the ocean ai challenge. *medRxiv*, pages 2024–04, 2024. 6
- [2] Babak Ehteshami Bejnordi, Mitko Veta, Paul Johannes Van Diest, Bram Van Ginneken, Nico Karssemeijer, Geert Litjens, Jeroen AWM Van Der Laak, Meyke Hermesen, Quirine F Manson, Maschenka Balkenhol, et al. Diagnostic assessment of deep learning algorithms for detection of lymph node metastases in women with breast cancer. *Jama*, 318(22):2199–2210, 2017. 6
- [3] Wouter Bulten, Kimmo Kartasalo, Po-Hsuan Cameron Chen, Peter Ström, Hans Pinckaers, Kunal Nagpal, Yuannan Cai, David F Steiner, Hester Van Boven, Robert Vink, et al. Artificial intelligence for diagnosis and gleason grading of prostate cancer: the panda challenge. *Nature medicine*, 28(1):154–163, 2022. 6
- [4] Gabriele Campanella, Matthew G Hanna, Luke Geneslaw, Allen Mirafior, Vitor Werneck Krauss Silva, Klaus J Busam, Edi Brogi, Victor E Reuter, David S Klimstra, and Thomas J Fuchs. Clinical-grade computational pathology using weakly supervised deep learning on whole slide images. *Nature medicine*, 25(8):1301–1309, 2019. 1
- [5] Richard J Chen, Chengkuan Chen, Yicong Li, Tiffany Y Chen, Andrew D Trister, Rahul G Krishnan, and Faisal Mahmood. Scaling vision transformers to gigapixel images via hierarchical self-supervised learning. In *Proceedings of the IEEE/CVF Conference on Computer Vision and Pattern Recognition*, pages 16144–16155, 2022. 1
- [6] Richard J Chen, Tong Ding, Ming Y Lu, Drew FK Williamson, Guillaume Jaume, Andrew H Song, Bowen Chen, Andrew Zhang, Daniel Shao, Muhammad Shaban, et al. Towards a general-purpose foundation model for computational pathology. *Nature Medicine*, 30(3):850–862, 2024. 1
- [7] Jonathan I Epstein, Lars Egevad, Mahul B Amin, Brett Delahunt, John R Srigley, Peter A Humphrey, Grading Committee, et al. The 2014 international society of urological pathology (isup) consensus conference on gleason grading of prostatic carcinoma: definition of grading patterns and proposal for a new grading system. *The American journal of surgical pathology*, 40(2):244–252, 2016. 8
- [8] Hossein Farahani, Jeffrey Boschman, David Farnell, Amirali Darbandsari, Allen Zhang, Pouya Ahmadvand, Steven JM Jones, David Huntsman, Martin Köbel, C Blake Gilks, et al. Deep learning-based histotype diagnosis of ovarian carcinoma whole-slide pathology images. *Modern Pathology*, 35(12):1983–1990, 2022. 6
- [9] Robert L Grossman, Allison P Heath, Vincent Ferretti, Harold E Varmus, Douglas R Lowy, Warren A Kibbe, and Louis M Staudt. Toward a shared vision for cancer genomic data. *New England Journal of Medicine*, 375(12):1109–1112, 2016. 6
- [10] Frederick M Howard, James Dolezal, Sara Kochanny, Galina Khramtsova, Jasmine Vickery, Andrew Srisuwananukorn, Anna Woodard, Nan Chen, Rita Nanda, Charles M Perou, et al. Integration of clinical features and deep learning on pathology for the prediction of breast cancer recurrence assays and risk of recurrence. *NPJ Breast Cancer*, 9(1):25, 2023. 1
- [11] Maximilian Ilse, Jakub Tomczak, and Max Welling. Attention-based deep multiple instance learning. In *International conference on machine learning*, pages 2127–2136. PMLR, 2018. 5
- [12] Guillaume Jaume, Paul Doucet, Andrew H Song, Ming Y Lu, Cristina Almagro-Pérez, Sophia J Wagner, Anurag J Vaidya, Richard J Chen, Drew FK Williamson, Ahron Kim, et al. Hest-1k: A dataset for spatial transcriptomics and histology image analysis. *arXiv preprint arXiv:2406.16192*, 2024. 2
- [13] Guillaume Jaume, Lukas Oldenburg, Anurag Vaidya, Richard J Chen, Drew FK Williamson, Thomas Peeters, Andrew H Song, and Faisal Mahmood. Transcriptomics-guided slide representation learning in computational pathology. In *Proceedings of the IEEE/CVF Conference on Computer Vision and Pattern Recognition*, pages 9632–9644, 2024. 3
- [14] Ren Yuan Lee, Chan Way Ng, Menaka Priyadharsani Rajapakse, Nicholas Ang, Joe Poh Sheng Yeong, and Mai Chan Lau. The promise and challenge of spatial omics in dissecting tumour microenvironment and the role of ai. *Frontiers in Oncology*, 13:1172314, 2023. 2

- [15] Jiayun Li, Wenyuan Li, Anthony Sisk, Huihui Ye, W Dean Wallace, William Speier, and Corey W Arnold. A multi-resolution model for histopathology image classification and localization with multiple instance learning. *Computers in biology and medicine*, 131:104253, 2021. 1
- [16] Geert Litjens, Peter Bandi, Babak Ehteshami Bejnordi, Oscar Geessink, Maschenka Balkenhol, Peter Bult, Altuna Halilovic, Meyke Hermesen, Rob Van de Loo, Rob Vogels, et al. 1399 h&e-stained sentinel lymph node sections of breast cancer patients: the camelyon dataset. *GigaScience*, 7(6):giy065, 2018. 6
- [17] Jianfang Liu, Tara Lichtenberg, Katherine A Hoadley, Laila M Poisson, Alexander J Lazar, Andrew D Cherniack, Albert J Kovatich, Christopher C Benz, Douglas A Levine, Adrian V Lee, et al. An integrated tcga pan-cancer clinical data resource to drive high-quality survival outcome analytics. *Cell*, 173(2):400–416, 2018. 7
- [18] Ming Y Lu, Bowen Chen, Drew FK Williamson, Richard J Chen, Ivy Liang, Tong Ding, Guillaume Jaume, Igor Odintsov, Long Phi Le, Georg Gerber, et al. A visual-language foundation model for computational pathology. *Nature Medicine*, 30(3):863–874, 2024. 6
- [19] Jiawei Ma, Po-Yao Huang, Saining Xie, Shang-Wen Li, Luke Zettlemoyer, Shih-Fu Chang, Wen-Tau Yih, and Hu Xu. Mode: Clip data experts via clustering. In *Proceedings of the IEEE/CVF Conference on Computer Vision and Pattern Recognition*, pages 26354–26363, 2024. 3
- [20] Jeffrey R Moffitt, Emma Lundberg, and Holger Heyn. The emerging landscape of spatial profiling technologies. *Nature Reviews Genetics*, 23(12):741–759, 2022. 1
- [21] Lambda Moses and Lior Pachter. Museum of spatial transcriptomics. *Nature methods*, 19(5):534–546, 2022. 1
- [22] Aaron van den Oord, Yazhe Li, and Oriol Vinyals. Representation learning with contrastive predictive coding. *arXiv preprint arXiv:1807.03748*, 2018. 3
- [23] Alec Radford, Jong Wook Kim, Chris Hallacy, Aditya Ramesh, Gabriel Goh, Sandhini Agarwal, Girish Sastry, Amanda Askell, Pamela Mishkin, Jack Clark, et al. Learning transferable visual models from natural language supervision. In *International conference on machine learning*, pages 8748–8763. PMLR, 2021. 3
- [24] Anjali Rao, Dalia Barkley, Gustavo S França, and Itai Yanai. Exploring tissue architecture using spatial transcriptomics. *Nature*, 596(7871):211–220, 2021. 2
- [25] Khadijeh Saednia, Andrew Lagree, Marie A Alera, Lauren Fleshner, Audrey Shiner, Ethan Law, Brianna Law, David W Dodington, Fang-I Lu, William T Tran, et al. Quantitative digital histopathology and machine learning to predict pathological complete response to chemotherapy in breast cancer patients using pre-treatment tumor biopsies. *Scientific Reports*, 12(1):9690, 2022. 1
- [26] Zhuchen Shao, Hao Bian, Yang Chen, Yifeng Wang, Jian Zhang, Xiangyang Ji, et al. Transmil: Transformer based correlated multiple instance learning for whole slide image classification. *Advances in neural information processing systems*, 34:2136–2147, 2021. 5
- [27] Huy V Vo, Vasil Khalidov, Timothée Darcet, Théo Moutakanni, Nikita Smetanin, Marc Szafraniec, Hugo Touvron, Camille Couprie, Maxime Oquab, Armand Joulin, et al. Automatic data curation for self-supervised learning: A clustering-based approach. *arXiv preprint arXiv:2405.15613*, 2024. 3
- [28] Xiyue Wang, Junhan Zhao, Eliana Marostica, Wei Yuan, Jietian Jin, Jiayu Zhang, Ruijiang Li, Hongping Tang, Kanran Wang, Yu Li, et al. A pathology foundation model for cancer diagnosis and prognosis prediction. *Nature*, pages 1–9, 2024. 1
- [29] Yanan Wang, Yu Guang Wang, Changyuan Hu, Ming Li, Yanan Fan, Nina Otter, Ikuan Sam, Hongquan Gou, Yiqun Hu, Terry Kwok, et al. Cell graph neural networks enable the precise prediction of patient survival in gastric cancer. *NPJ precision oncology*, 6(1):45, 2022. 1
- [30] F Alexander Wolf, Philipp Angerer, and Fabian J Theis. Scanpy: large-scale single-cell gene expression data analysis. *Genome biology*, 19:1–5, 2018. 5
- [31] Ronald Xie, Kuan Pang, Sai Chung, Catia Perciani, Sonya MacParland, Bo Wang, and Gary Bader. Spatially resolved gene expression prediction from histology images via bimodal contrastive learning. *Advances in Neural Information Processing Systems*, 36, 2024. 3, 5
- [32] Hanwen Xu, Naoto Usuyama, Jaspreet Bagga, Sheng Zhang, Rajesh Rao, Tristan Naumann, Cliff Wong, Zelalem Gero, Javier González, Yu Gu, et al. A whole-slide foundation model for digital pathology from real-world data. *Nature*, pages 1–8, 2024. 1, 6
- [33] Zhenzhen Xun, Xinyu Ding, Yao Zhang, Benyan Zhang, Shujing Lai, Duowu Zou, Junke Zheng, Guoqiang Chen, Bing Su, Leng Han, et al. Reconstruction of the tumor spatial microenvironment along the malignant-boundary-nonmalignant axis. *Nature Communications*, 14(1):933, 2023. 2
- [34] Claire S Zhu, Paul F Pinsky, Barnett S Kramer, Philip C Prok, Mark P Purdue, Christine D Berg, and John K Gohagan. The prostate, lung, colorectal, and ovarian cancer screening trial and its associated research resource. *Journal of the National Cancer Institute*, 105(22):1684–1693, 2013. 6

SPADE: Spatial Transcriptomics and Pathology Alignment Using a Mixture of Data Experts for an Expressive Latent Space

Supplementary Material

S6. Datasets

We provide descriptions of the datasets used for the evaluation of SPADE.

NSCLC For the non-small cell lung carcinoma (NSCLC) subtyping task, we utilize H&E WSIs from the PLCO and CPTAC datasets to classify cases of lung adenocarcinoma (LUAD) and lung squamous cell carcinoma (LUSC). The PLCO cohort contains 589 slides from 274 patients (LUAD: 171, LUSC: 103). The CPTAC cohort contains 1331 slides from 427 patients (LUAD: 219, LUSC: 208). We perform a patient-level, label-stratified split of both cohorts into training, validation, and test sets with a 70:10:20 ratio. Performance was evaluated using AUCROC and F1-Score.

We also ran a lung cancer survival task using the same PLCO lung cohort. Mortality status from the PLCO study data is used to determine survival, censorship, and duration of survival for this dataset. Out of 274 participants, 213 survived. We performed a patient-level, label-stratified split into training, validation, and test sets with a 70:10:20 ratio. Performance was evaluated using the c-index.

PANDA For the prostate cancer ISUP grading task, we utilized 10,616 core needle biopsy cases collected from Karolinska Institute and Radboud University Medical Center. All biopsy WSIs were obtained from the Prostate Cancer Grade Assessment (PANDA) challenge. Each biopsy is assigned an ISUP grade on a scale from 1 to 5 if cancerous, while benign biopsies receive a label of 0, resulting in a six-class classification problem. The class distribution is as follows: class 0 (2892), class 1 (2666), class 2 (1343), class 3 (1242), class 4 (1249), and class 5 (1224). Patient identification information was not provided in the dataset, so patient-level splits could not be created. Instead, we perform a label-stratified split into training, validation, and test sets with a 70:10:20 ratio. Performance was evaluated using AUCROC and macro F1-Score.

Camelyon16 We used the CAMELYON16 dataset, which includes 397 WSIs from sentinel lymph node biopsies, to detect metastases in breast cancer patients. Metastases are categorized into three classes—'negative' (237), 'micro' (80), and 'macro' (80)—making this a three-class classification problem. Patient identification information was not provided in the dataset, so patient-level splits could not be created. Instead, we perform a label-stratified split into training, validation, and test sets with a 70:10:20 ratio. Performance was evaluated using AUCROC and macro F1-

Score.

UBC-OCEAN For ovarian cancer subtype classification, we utilized 513 biopsy samples from the UBC ovarian cancer subtype classification and outlier detection (UBC-OCEAN) competition. Each sample is assigned one out of five histological subtypes of ovarian cancer: class 0 (217), class 1 (42), class 2 (119), class 3 (94), and class 4 (41). Patient identification information was not provided in the dataset, so patient-level splits could not be created. Instead, we perform a label-stratified split into training, validation, and test sets with a 70:10:20 ratio. Performance was evaluated using AUCROC and macro F1-Score.

Breast For the breast cancer subtyping task, we used the PLCO Breast dataset. The PLCO cohort consists of 1768 slides from 867 patients. Each sample is categorized into one of three classes - 'lobular' (104), 'ductal' (657), and 'other' (106). We perform patient-level, label-stratified split into training, validation, and test sets with a 70:10:20 ratio. Performance was evaluated using AUCROC and macro F1-Score.

We use the PLCO Breast and TCGA-BRCA datasets for breast cancer survival tasks. Mortality status from the PLCO study data is used to determine survival, censorship, and duration of survival. Out of 867 participants, 552 survived. The TCGA-BRCA dataset consists of 1267 WSIs spanning 1042 patients, with 963 surviving based on disease-specific survival (DSS) status. We perform a patient-level, label-stratified split for both datasets into training, validation, and test sets with a 70:10:20 ratio. Performance was evaluated using the c-index.

Prostate For our prostate cancer biochemical recurrence (BCR) tasks, we use an in-house dataset of radical prostatectomy whole-mount WSIs and the TCGA-PRAD dataset. The in-house dataset spans 161 patients, with one whole-mount WSI selected per patient based on pathology reports. The ratio of patients without BCR versus those with BCR is 135:26. The Gleason grading breakdown of this dataset is: 74 - 3+4 cases, 46 - 4+3 cases, 20 - 4+5 cases, 13 - 3+3 cases, 6 - 4+4 cases, 1 - 3+5 case, and 1 - 5+4 case. The TCGA-PRAD dataset consists of 336 WSIs spanning 322 patients with a BCR rate ratio of 285:37. We perform a patient-level, label-stratified split into training, validation, and test sets with a 70:10:20 ratio for both in-house and TCGA-PRAD datasets. Performance was evaluated using the c-index.

Uterine For the uterine cancer survival task, we use the TCGA-UCEC dataset. The dataset consists of 786 images spanning 504 patients, with 445 out of the 504 patients total surviving. We perform a patient-level, label-stratified split into training, validation, and test sets with a 70:10:20 ratio. Performance was evaluated using the c-index.

S7. Model and training

For pretraining training, we employ a weight decay of 1×10^{-5} and use the AdamW optimizer with a learning rate of 1×10^{-4} , along with a cosine decay scheduler. For the slide classification experiments, we utilized a cross-entropy loss. We employed early stopping if the validation loss failed to improve over ten consecutive epochs with a total training epochs of 20. For survival prediction experiments, we used negative log-likelihood loss (NLL).

ABMIL downstream architecture: ABMIL architecture used in the downstream experiments consists of three components. First, a 2-layer MLP with 256 or 512 hidden units, layer normalization, ReLU activation, and 0.25 dropout. This is followed by a gated-attention network consisting of 2-layer MLP, with Sigmoid and Tanh activation, respectively, and 0.25 dropout. Finally, a post-attention linear classification layer with 256 or 512 hidden units is applied.

TransMIL downstream architecture: TransMIL architecture was used in the downstream experiments. The core of the TransMIL architecture features two Transformer layers, both configured with a hidden dimension of 256 or 512. After these Transformer layers, a layer normalization step is applied with a dimensionality of 256 or 512. Finally, the architecture includes a classification layer and a linear transformation mapping from 256 or 512 features to the number of target classes.

TANGLE downstream architecture: For the TANGLE baseline, we employed LogisticRegression following the open-source instructions provided by the authors.

S8. Clustering

For the proposed 2-step clustering, the size of the uniform sample \mathcal{D}_i^t is 1,500,000 patches. The fine-grained K-means is performed over each \mathcal{D}_i^t with $k = 16$. A second round of clustering is performed on top of previously found clusters S with $k = 16$.

In the first clustering step, we performed clustering within each tissue type, varying k across a range of values. To determine the optimal number of clusters, we calculated the within-cluster sum of squares (WCSS) and applied the elbow method. The corresponding elbow plot (see Figure S3), suggests that the optimal choice is $k = 16$, as improvements in WCSS diminish beyond this point. A secondary drop is

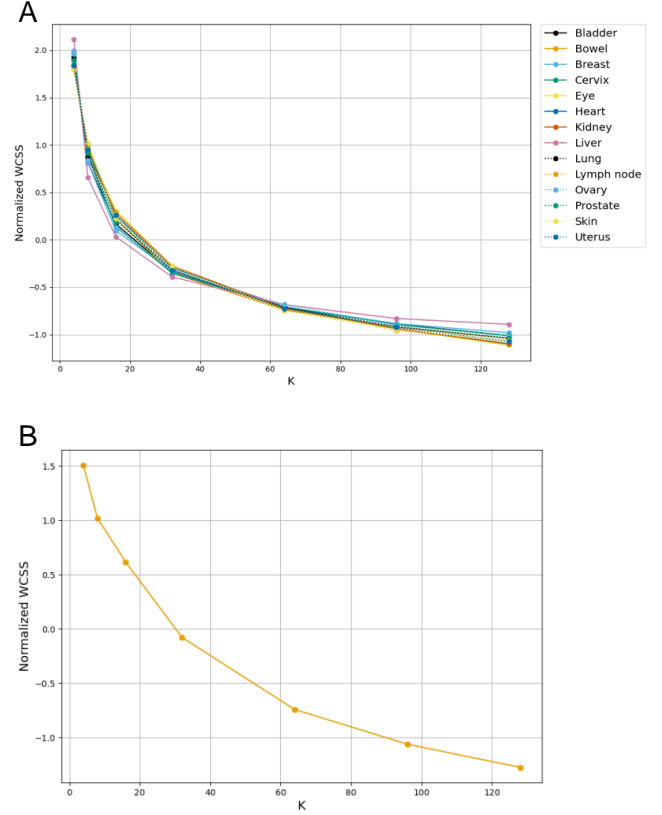


Figure S3. **Within-Cluster Sum of Squares (WCSS) Elbow Plots Across Values of K** **A.** First-level clustering performance evaluated using normalized WCSS across 14 organs. **B.** Second-level clustering performance evaluated using normalized WCSS.

observed at $k = 32$, which we included in our ablation studies to assess its impact on downstream task performance.

In the second clustering step, we clustered the centroids obtained prior to form broader, overall clusters. Again, we evaluated values of k using WCSS and generated an elbow plot (see Figure S3). In this case, the distinction between $k = 16$ and $k = 32$ is less pronounced. However, given the higher computational cost of running 32 experts, we opted for $k = 16$ to reduce overall model complexity. This approach allowed us to structure the data efficiently while balancing computational cost and cluster granularity.

S9. Additional experiments

We implemented a version of SPADE using clusters generated from the first stage of our two-step clustering algorithm, where each organ-specific cohort was clustered with $k = 16$, totaling 240 cluster centroids and, in turn, 240 experts. We report the classification results for two subtyping tasks: Camelyon16 and CPTAC lung.

	Lung		Lymph Nodes	
	CPTAC		Camelyon	
	AUC	F1	AUC	F1
SPADE+ABMIL	96.6	89.7	93.6	77.6
SPADE+TransMIL	96.0	89.3	91.1	68.9

Table S7. **One-step clustering for the mixture of experts.** We compare the performance of SPADE with 240 data experts using two subtyping tasks. Metrics AUC and F1 are shown as percentages.

We observe that data experts trained on cluster centroids obtained with a two-step clustering approach lead to better results compared to a one-step clustering approach (Table S7). The one-step approach results in a reduction in AUC for the CPTAC dataset, with decreases of 1.9% for SPADE+ABMIL and 0.62% for SPADE+TransMIL, and for the Camelyon dataset, with decreases of 5.68% for SPADE+ABMIL and 2.46% for SPADE+TransMIL. F1 values decreased by 3.03% for SPADE+ABMIL and 0.45% for SPADE+TransMIL on the CPTAC dataset. For the Camelyon dataset, F1 values dropped by 12.91% for SPADE+ABMIL and 16.91% for SPADE+TransMIL. This can be explained by the fact that one-step clustering leads to cluster centers that are not sufficiently representative of a specific tissue prototype and, therefore, cannot learn a good representation.

To further evaluate the effectiveness of SPADE, we conducted an experiment comparing its performance against a single-expert model (SPADE-0) across subtyping, survival and BCR prediction tasks. As shown in Tables S8, S9, SPADE consistently outperformed SPADE-0 in most datasets, demonstrating the advantage of incorporating multiple experts tailored to different tissue types.

S10. Limitations

While we trained on the largest and most diverse public Visium dataset available, the sample size 515 remains small compared to large digital pathology datasets. However, given the cost of acquiring spatial transcriptomics data and the relative novelty of the technique, it may be some time before datasets of comparable size to digital pathology collections can be assembled.

Spatial transcriptomics is an exciting new technique, but it has several limitations due to the novelty of the platforms used for data acquisition. Spatial transcriptomics gene expression data often suffers high dropout rates, with many genes showing expression levels of zero and other noise-related issues. Although we attempted to mitigate this issue by clustering in the image space and using it to supervise our data experts, incorporating additional supervision using

the gene expression space could enhance model robustness and leverage this data type even more.

HEST-1k contains various types of spatial transcriptomics data, spanning in-situ imaging techniques (e.g., Xenium) and Next-Generation sequencing techniques (e.g., Visium). In our study, we choose only to use the Visium data, as it provides the whole genome transcriptome, enabling us to identify sets of highly variable gene sets shared across tissue types without being restricted by organ-specific panels. In future work, we plan to incorporate other spatial transcriptomics data sets and expand our dataset further.

Lastly, our method relies on a 2-step K-means clustering procedure, which is sensitive to the choice of K. It is challenging to know what K is optimal for all downstream tasks, and we did not try optimizing different values of K for our first or second step. We also did not attempt other clustering algorithms, which could also impact performance. We leave this analysis for future studies.

	Lung				Prostate				Lymph Nodes	Ovarian	Breast			
	PLCO		CPTAC		PANDA		TCGA- PRAD		CAM16	UBC- OCEAN	PLCO		TCGA- BRCA	
	AUC	F1	AUC	F1	AUC	F1	AUC	F1	AUC	F1	AUC	F1	AUC	F1
SPADE-0+ABMIL	96.1	93.3	<u>96.3</u>	87.4	<u>93.6</u>	<u>66.8</u>	<u>81.5</u>	39.6	<u>97.1</u>	<u>85.1</u>	<u>97.1</u>	<u>85.7</u>	<u>78.7</u>	59.2
SPADE+ABMIL	98.5	<u>87.1</u>	97.9	92.5	94.9	74.7	82.1	56.9	98.6	89.1	97.8	87.1	82.1	<u>57.3</u>
SPADE-0+TransMIL	96.5	85.0	93.2	79.4	92.5	66.5	71.8	<u>44.0</u>	95.2	<u>85.5</u>	94.1	79.7	57.0	48.4
SPADE+TransMIL	<u>96.6</u>	82.0	<u>96.3</u>	<u>89.7</u>	91.7	62.5	72.0	43.9	93.4	82.9	<u>97.3</u>	83.1	72.5	47.9
													97.3	<u>97.5</u>

Table S8. Comparison of mixture-of-experts (SPADE) to single expert (SPADE-0) for subtyping task. Metrics AUC and F1 are shown as percentages.

	Prostate BCR		Lung	Uterine	Breast	
	Private	TCGA-PRAD	PLCO	TCGA-UCEC	TCGA-BRCA	PLCO
	c-index	c-index	c-index	c-index	c-index	c-index
SPADE-0+ABMIL	0.650	0.589	0.572	0.701	0.685	0.561
SPADE+ABMIL	<u>0.670</u>	<u>0.594</u>	<u>0.647</u>	0.724	<u>0.718</u>	0.595
SPADE-0+TransMIL	0.655	0.595	0.566	0.708	0.689	0.555
SPADE+TransMIL	0.714	0.588	0.723	<u>0.710</u>	0.730	<u>0.574</u>

Table S9. Comparison of mixture-of-experts (SPADE) to single expert (SPADE-0) for survival and BCR. c-index values are shown as percentages.